ELECTROCHEMISTRY

A physical catalyst for the electrolysis of nitrogen to ammonia

Yang Song,[1] Daniel Johnson,[1] Rui Peng,[1] Dale K. Hensley,[1] Peter V. Bonnesen,[1] Liangbo Liang,[1] Jingsong Huang,[1,2] Fengchang Yang,[3] Fei Zhang,[3] Rui Qiao,[3] Arthur P. Baddorf,[1] Timothy J. Tschaplinski,[4] Nancy L. Engle,[4] Marta C. Hatzell,[5] Zili Wu,[1,6] David A. Cullen,[7] Harry M. Meyer III,[7] Bobby G. Sumpter,[1,2] Adam J. Rondinone[1]*

Ammonia synthesis consumes 3 to 5% of the world's natural gas, making it a significant contributor to greenhouse gas emissions. Strategies for synthesizing ammonia that are not dependent on the energy-intensive and methane-based Haber-Bosch process are critically important for reducing global energy consumption and minimizing climate change. Motivated by a need to investigate novel nitrogen fixation mechanisms, we herein describe a highly textured physical catalyst, composed of N-doped carbon nanospikes, that electrochemically reduces dissolved N_2 gas to ammonia in an aqueous electrolyte under ambient conditions. The Faradaic efficiency (FE) achieves 11.56 ± 0.85% at −1.19 V versus the reversible hydrogen electrode, and the maximum production rate is 97.18 ± 7.13 μg hour^{-1} cm^{-2}. The catalyst contains no noble or rare metals but rather has a surface composed of sharp spikes, which concentrates the electric field at the tips, thereby promoting the electroreduction of dissolved N_2 molecules near the electrode. The choice of electrolyte is also critically important because the reaction rate is dependent on the counterion type, suggesting a role in enhancing the electric field at the sharp spikes and increasing N_2 concentration within the Stern layer. The energy efficiency of the reaction is estimated to be 5.25% at the current FE of 11.56%.

INTRODUCTION

Worldwide production of ammonia exceeds 145 million metric tons annually (*1*). The Haber-Bosch process must be performed at high temperature and pressure using pure hydrogen, which is usually sourced from natural gas via steam reforming; hence, ammonia production represents a significant contributor to climate change. Because of this, alternative methods for synthesizing ammonia are now of great scientific interest (*2*–*5*). Although the literature is still sparse, a number of electrocatalytic studies that produce NH_3 directly via electroreduction of N_2 and water or steam have been reported (*6*). Most studies on electrochemical production of ammonia are based on solid-state electrolytes at elevated temperature and pressure (*7*). Other studies have also been reported on the basis of liquid electrolytes, such as organic solvents (*8*), ionic liquids (*9*), molten salts (*10*, *11*), aqueous electrolyte at elevated (*12*) or ambient pressure (*13*), or fullerene electrodes with aqueous electrolyte (*14*). In these studies, transition metal complexes and materials are often exploited as the catalysts.

Aqueous electrolyte approaches promise simplicity and low cost, as the solvent water directly becomes the hydrogen source. However, aqueous electrolyte approaches suffer from competitive hydrogen evolution that limits overall efficiency, causing a low overall reaction rate. To date, the highest reported Faradaic efficiency (FE) for an aqueous reaction under ambient conditions is 1.3% (*6*). There is no report yet on alternative catalysts that allow one to abandon the conventional transition metal catalysts as a result of significant improvements of electrocatalytic performance. Carbon-based catalysts could be attractive alternatives to transition metal catalysts for electrolytic ammonia synthesis because of low selectivity for hydrogen evolution. We previously reported a new carbon-based catalyst composed of nitrogen-doped carbon nanospikes (CNSs; fig. S1) that exhibit low hydrogen selectivity and high surface area, making it suitable for complex electrocatalytic reactions such as oxygen (*15*) and CO_2 reduction (*16*). Here, we describe the application of CNS as the electrode material for the electrochemical reduction of dissolved nitrogen gas to ammonia.

RESULTS AND DISCUSSION

Materials and electrochemistry

Unlike typical carbon electrode materials, the CNS surface features a unique morphology of abundant-oriented nanospikes approximately 50 to 80 nm in length, where each nanospike consists of layers of carbon ending in a ~1-nm-wide sharp tip (Fig. 1A and fig. S1) (*15*). We expected that the sharp tips in the CNS would markedly amplify the local electric field. A simple estimate using an exohedral electric double-sphere capacitor model (*17*) along with atomistic simulations for strongly curved surfaces with positive curvatures (figs. S2 and S3) confirmed that the electric field at the tip's surface increases as the tip radius reduces. For a tip with a radius of 1 nm and a voltage drop of 1.8 V (potential difference between the polarized CNS electrode and the bulk electrolyte; see the Supplementary Materials), the electric field on its surface enhances by 2 V/nm compared to that near a planar electrode surface. For smaller tip radii (fig. S2), the enhancement of electric field can be even stronger. It has long been hypothesized that strong electric fields may serve as "physical catalysts" for chemical processes including ammonia synthesis by influencing N_2's molecular orbital energy levels (*18*). Other recent work demonstrates that a high electric field may increase reagent concentration near the tips of gold needle electrodes (*19*). Here, we investigated the possibility of using the phenomenon of physical catalysis with a carbon-based electrode featuring sharp spikes and containing nitrogen doping but no metal elements for the electrocatalytic fixation of N_2.

[1]Center for Nanophase Materials Sciences, Oak Ridge National Laboratory, Oak Ridge, TN 37831, USA. [2]Computational Sciences and Engineering Division, Oak Ridge National Laboratory, Oak Ridge, TN 37831, USA. [3]Virginia Polytechnic Institute and State University, Blacksburg, VA 24061, USA. [4]Biosciences Division, Oak Ridge National Laboratory, Oak Ridge, TN 37831, USA. [5]George W. Woodruff School of Mechanical Engineering, Georgia Institute of Technology, Atlanta, GA 30332, USA. [6]Chemical Sciences Division, Oak Ridge National Laboratory, Oak Ridge, TN 37831, USA. [7]Materials Science and Technology Division, Oak Ridge National Laboratory, Oak Ridge, TN 37831, USA.
*Corresponding author. Email: rondinoneaj@ornl.gov

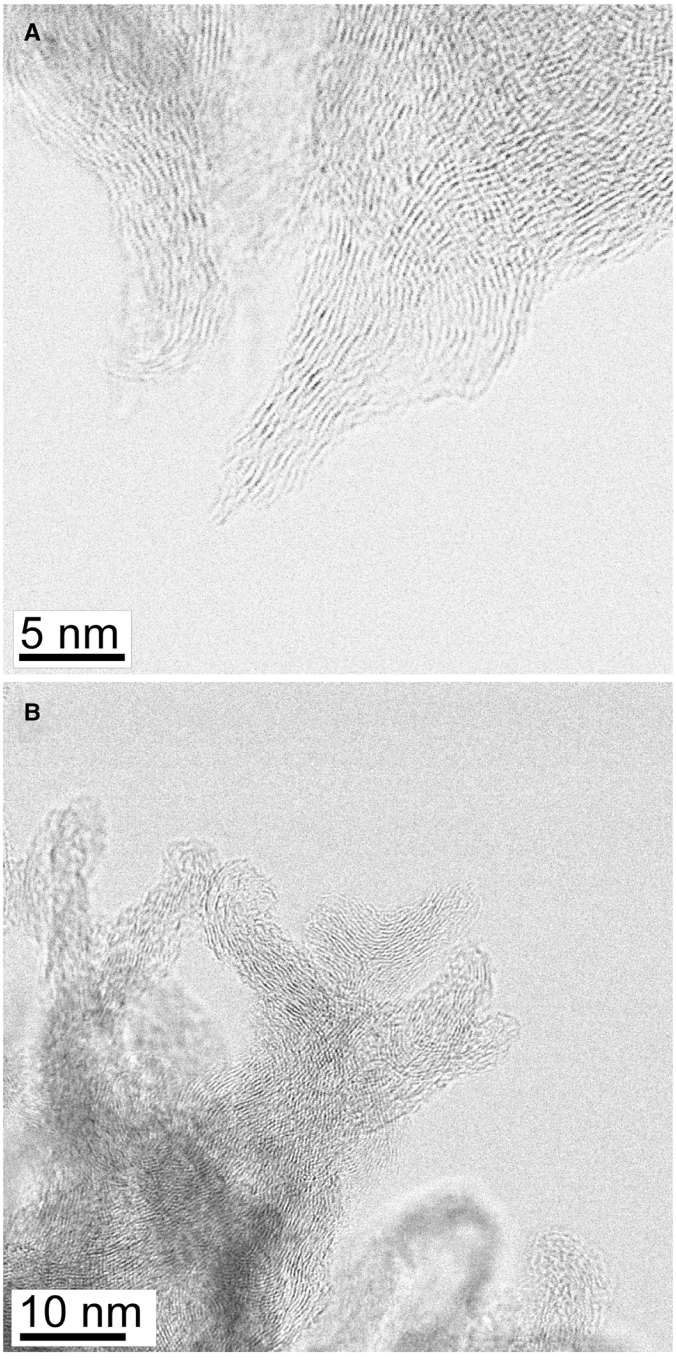

Fig 1. Aberration-corrected scanning transmission electron microscopy (STEM) images of CNSs. (**A**) The pristine nanospikes exhibit layers of folded graphene with some structural disorder due to nitrogen incorporation in the basal plane. (**B**) O-etched CNS retains the layered graphene structure but exhibits a much larger radius at the tip, thereby lowering the local electric field present at the tips.

Electrochemistry was performed at ambient temperature and pressure, using CNS for the cathode and 0.25 M aqueous $LiClO_4$ solution for the electrolyte. We chose $LiClO_4$ for its electrochemical stability and because of previous reports of enhanced interactions between Li^+ and N_2 (*20*, *21*). We used multiple controls, including identical experiments on oxygen plasma–etched (O-etched) CNS that contained the same amount of nitrogen dopants as CNS (table S1) but had the sharp tip texture fully etched away (Fig. 1B) so that it would not produce the same high electric fields as CNS. Glassy carbon was also chosen as a control because it lacked both nitrogen dopants and texture. Last, experiments were conducted with pristine CNS in argon-saturated electrolyte as a control. Counterion effects were evaluated by comparison with other electrolytes containing $NaClO_4$ and $KClO_4$.

Chronoamperometry (CA) measurements were conducted for 6 hours each over a potential range of −0.79 to −1.29 V versus reversible hydrogen electrode (RHE), a range based on the linear sweep voltammetry profile. A new electrode was used for each measurement, and the ammonia product was quantified using a quantification protocol based on U.S. Environmental Protection Agency (EPA) Standard Method 350.1 (indophenol colorimetry; fig. S4). Stability was evaluated over 6-hour (figs. S5 to S7) and 100-hour experiments (fig. S8). In all of the experiments, the integrated current and partial current of ammonia formation are linear with time, which indicates that ammonia was produced continuously by the electrochemical reaction. As shown in fig. S8, the overall current density is stable at the highest production rate of the 100-hour experiment. The periodic noises were caused during sampling of the electrolyte to measure the rate of ammonia formation. The formation rate started at about ~90 μg $hour^{-1}$ cm^{-2} at −1.19 V versus RHE, climbed to ~100 μg $hour^{-1}$ cm^{-2} by 10 hours, and remained at 100 ± 5 μg $hour^{-1}$ cm^{-2} for the remainder of the experiment. The total current density, which includes hydrogen evolution in addition to ammonia production, increased slightly up to 40 hours and then remained stable. This slight increase is possibly due to mild oxidation, which increases wettability of the CNS surface, a phenomenon that has been noted on other N-doped carbon catalysts (*22*). To rule out the possibilities that Ag or Pt might leach out of the reference electrode (*23*) or from the counter electrode and get deposited on the working electrode during this extended experiment, thereby increasing H_2 evolution and contributing to the increased current density as shown in fig. S8, we performed x-ray photoelectron spectroscopy (XPS) measurements on the electrode after the electrolysis. No evidence of Ag or Pt was observed on the electrode after the experiment.

A chronopotentiometry (CP) experiment on a larger (4.8 cm^2) electrode was also carried out to investigate stability during the first 5 hours of the reaction. Figure S9 illustrates the change in potential necessary to maintain a set total current density of 1.25 mA cm^{-2}. In this experiment, the potential drops after initial charging and slowly decreases for 4 hours. At hour 4, the potential begins to rise to maintain the set current density, which is possibly due to suppressed hydrogen evolution as a result of rising local pH near the electrode surface. That interpretation is supported by the consistent production rate of ammonia, observable in the 100-hour CA experiment (fig. S8) and the CP experiment (fig. S9).

The rate of ammonia formation (R_{NH3}; Fig. 2A) on CNS increased with increasing negative potential to −1.19 V, where a maximum rate (R_{NH3}, 97.18 ± 7.13 μg $hour^{-1}$ cm^{-2}) was achieved, and above which the rate declined because of the competitive formation of hydrogen gas (*24*, *25*). The FE at −1.19 V is 11.56 ± 0.85 % (Fig. 2B), which is significantly higher than other aqueous electrochemical approaches albeit lower than that achieved by molten salt electrolysis (*10*). The three controls (O-etched CNS, glassy carbon, and Ar with CNS) produced very little or no ammonia at each voltage (Fig. 2, A and B, and table S2). Although the O-etched control has some texture [scanning electron microscopy (SEM); fig. S10], its reactivity is only slightly improved over

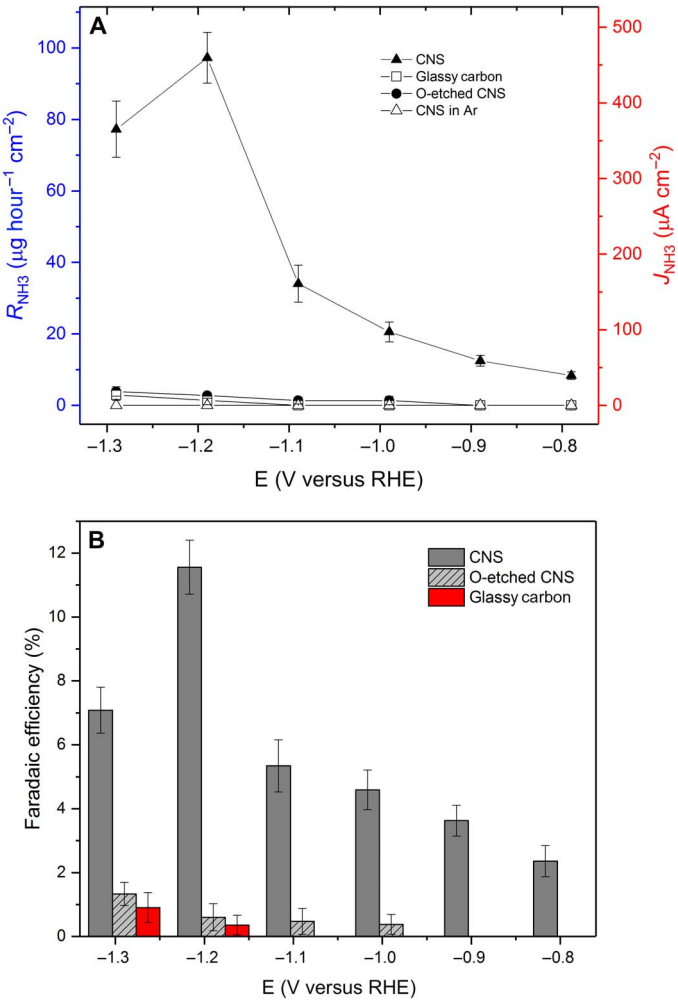

Fig. 2. The partial current densities and formation rate of ammonia normalized by the ECSA at various potentials in a range from −1.29 to −0.79 V using 0.25 M $LiClO_4$ electrolyte. (**A**) The CNS electrode in the presence of N_2 produced significant ammonia compared to O-etched CNS and glassy carbon controls or to an argon gas experiment, which produced no ammonia. The formation rate increased to −1.19 V, above which hydrogen formation outcompeted ammonia formation. The partial current densities and formation rate of ammonia were normalized by the ECSA. (**B**) The Faradaic efficiencies reflect the formation rates, with the highest efficiency of 11.56 ± 0.85% at −1.19 V. For both (A) and (B), error bars represent the SD of all measurements at that potential.

the glassy carbon control. The sharp contrast between these two controls and the CNS indicates that the spike texture is much more important to the reactivity than the electrochemical surface area (ECSA) or the N-doping, consistent with our hypothesis that electroreduction of N_2 is driven by the strong electric fields derived from the sharp tips of the CNS. When N_2 gas is removed and replaced with argon, then no ammonia is formed. We performed CNS in N_2 experiments at least three times, each with a new electrode, and six times for the critical potential of −1.19 V. The complete data for partial current densities for all samples and controls are presented in table S2. Note that the current densities are unoptimized and still much below the level that would be required for commercial application.

Electric field effects

Because nitrogen is required for the plasma-enhanced chemical vapor deposition (PECVD) synthesis of CNS (*15*), each CNS sample always contains approximately 5% N dopants (table S1). Although N-doping is not as critical as the texture for N_2 electroreduction (Fig. 2), it functions to raise the Fermi level of the CNS above that of glassy carbon (*26*), thereby allowing N_2 reduction to proceed by a lower polarization on the cathode (the difference between the electrode's open-circuit potential ϕ_o and the polarized potential ϕ_p). The open-circuit pontentials measured for the unetched and O-etched CNS are −0.16 V lower than that of glassy carbon, reflecting the elevated Fermi level (table S3). Consequently, the N-doped materials are subjected to smaller polarizations compared to glassy carbon toward the electrode potential that yields the maximal NH_3 production rate (table S3). However, only the pristine CNS of the two N-doped materials is able to effectively reduce N_2 to NH_3. Therefore, we focus on the strong electric field induced by the sharp spikes, unique to the pristine CNS materials, which may promote a physical catalytic reaction mechanism.

The electrochemical reactions can be summarized in the following general scheme (*6*, *13*). On the cathode, N_2 is electrochemically reduced to ammonia in the presence of water

$$N_2 + 6H_2O + 6e^- \rightarrow 2NH_3 + 6OH^- \quad (1)$$

On the anode, hydroxide is electrochemically oxidized to oxygen gas

$$6OH^- \rightarrow 3/2O_2 + 3H_2O + 6e^- \quad (2)$$

and the overall cell reaction is therefore

$$N_2 + 3H_2O \rightarrow 2NH_3 + 3/2O_2 \quad (3)$$

Unlike the Haber-Bosch process, this reaction can be viewed as a competition for hydrogen between N_2 and O_2, leading to the formation of NH_3 going forward or H_2O going backward. Because the forward reaction has a positive standard Gibbs energy change of $\Delta G° = +339.3$ kJ mol^{-1} of NH_3, the electroreduction of N_2 in water to form NH_3 is equivalent to an energy storage process.

For the reaction mechanism, N_2 reduction to ammonia on a heterogeneous surface can proceed by a dissociative or an associative mechanism (*6*, *27*). In the former case, the triple bond in N_2 is broken, giving two surface-bound N atoms before hydrogenations take place. In the latter case, the N_2 molecule, usually adsorbed on a surface, can be hydrogenated without needing to first break the triple bond in N_2. For N_2 fixation catalyzed by transition metal surfaces, for example, in the Haber-Bosch process at high temperature, the reaction involves a dissociative mechanism whereby hydrogenation takes place on surface-bound N atoms (*28*–*30*). However, recent theoretical evaluations of electrocatalysts for N_2 reduction at ambient conditions indicated that the dissociative mechanism is only possible on early transition metals but impossible on late transition metals at room temperature (*27*). In comparison, the electrolysis on the CNS electrode takes place at room temperature in the absence of any transition metals. Therefore, it is reasonable to assume that the N_2 reduction on CNS should proceed according to an associative mechanism.

The difference in NH_3 formation rate between the unetched CNS and its two control electrode materials resides in the sharp spikes with tip size down to 1 nm. This prompts us to hypothesize a causality chain from the sharp spikes on CNS, the enhanced local electric field at the tip of CNS, and the facilitated N_2 electroreduction, to the promoted

ammonia production. Assuming an associative mechanism, the cathode reaction shown in Eq. 1 for CNS should proceed through six sequential coupled electron and proton transfers from the electrode and electrolyte, respectively (*6*, *31*). Because of its inert nature, herein, we explore the possibility of N_2 reduction at the first step, that is, the first electron acquisition under a strong electric field. The influence of an electric field on a N_2 molecule has been previously examined theoretically, showing that the polarization of N_2 in an external electric field leads to enhanced dipole moment, elongated bond length, and weakened bond strength (*18*, *32*). Furthermore, the molecular orbital levels (for example, $2\sigma_g$ and $2\sigma_u$ and also the remaining levels) of N_2 were found to decrease linearly with the strength of a longitudinal electric field (*18*). This observation is confirmed by our high-level electron propagator theory (EPT) calculations (see the Supplementary Materials) for a N_2 molecule in a longitudinal and transversal electric field of variable strengths (fig. S11). Although these calculations did not take solvation effect into account, the trends reflect profound implications for an enhanced reactivity of an otherwise inert N_2 molecule in the presence of the strong electric field. On the basis of N_2's orbital levels calculated by EPT, and following Koopmans' theorem (*33*), it becomes energetically favorable to reduce N_2 by injecting electrons into the antibonding orbitals of N_2 under strong applied electric field (see the Supplementary Materials). In comparison, the electric field induced by two of the controls, the O-etched CNS or the glassy carbon film electrode, will be much weaker and therefore not likely to facilitate the electroreduction of N_2, limiting the ammonia production rate.

Work function measurements

To better understand the role of the material texture and electrode polarization in assisting N_2 reduction, we measured the work functions (WFs) of pristine CNS emersed from electrolyte using an ultraviolet photoelectron spectrometer (UPS), according to the general technique of Hansen and co-workers (*34*, *35*). Pristine CNS electrodes were emersed from N_2-saturated $LiClO_4$ electrolyte at a range of potentials, from open-circuit (+0.38 V) down to slightly below operational (−1.29 V, RHE) and measured using UPS (example spectrum in fig. S12A and WF data in fig. S12B). The data are noisy at potentials lower than −0.9 V, which reflects the fact that hydrogen evolution is occurring at these more negative potentials and that the double layer is turbulent; hence, a repeat experiment was conducted at a few critical voltages in that range. The spectra were typical, with an obvious low-energy cutoff, although, in occasional samples, we observed a second lower-energy peak (fig. S12A), which complicated the WF measurements (the lower-energy peak is shown as separate data points in fig. S12B). As discussed in more detail below, the lower-energy peak may be ascribed to emission from the nanospike tips, whereas the higher-energy shoulder is from surrounding carbon. However, the WF exhibits a general trend of decrease with increasing negative emersion potential. The decrease is not 1:1 eV/V applied, as observed for metallic electrodes (*35*, *36*), nor is it linear. This observation could reflect the difficulty in retaining an intact emersed double layer when the first lithium ion layer is merely physisorbed and still in a hydrated state, which would be expected at more positive potentials. At more negative potentials in our atomistic simulations, the lithium layer is dehydrated, and perhaps chemisorbed, and could therefore be better preserved during the WF measurement.

Note that the bulk of the literature for emersed electrodes, including the original work of Hansen *et al.* (*34*), has focused on metallic electrodes under anodic conditions, with adsorbed anions being of interest rather than adsorbed cations. Metals typically experience a one-to-one change in WF with emersed potential (*35*, *36*), which plateaus according to the maximum potential that can be applied before double-layer breakdown. Although literature data for carbons are sparser, the change in WF is generally consistent with that normally seen for metals. It is clear that the CNS/electrolyte system has a significantly reduced WF (3.19 eV if the higher energy shoulder is used and 2.61 eV if the lower energy shoulder is used) with electrode polarizations, which supports enhanced reduction capability of CNS for electron injection under operating conditions.

We also measured the WFs of unemersed CNS, O-etched CNS, and the glassy carbon control in a vacuum. The UPS spectrum of pristine, unemersed CNS is complex and appears to contain contributions from both the sharp tips and the surrounding CNS surface. There is a large emission at very low energy, so that the low-energy cutoff in the spectrum was below the minimal detection energy for our hemispherical electron detector, even with an applied potential of −4.5 V to shift emitted electrons to higher energy (fig. S13). Because of this low-energy emission, the absolute WF of the sharp tips for pristine, unemersed CNS could not be measured reliably using this technique. The spectrum for

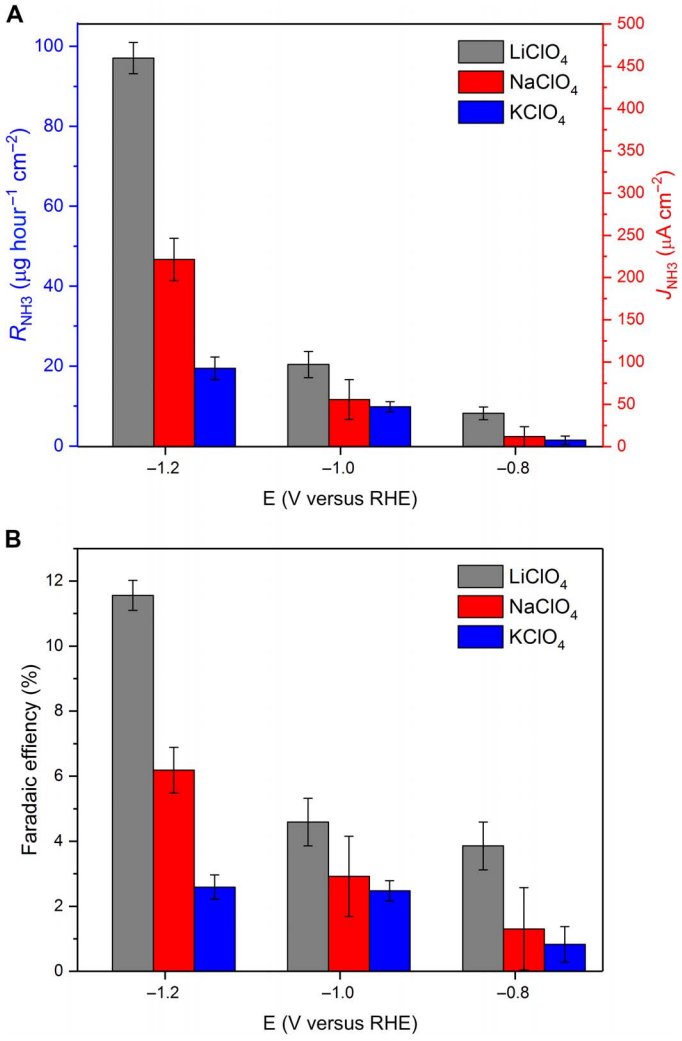

Fig. 3. Comparison of electrolyte counterion effect of Li^+ (gray), Na^+ (red), and K^+ (blue). (**A**) The formation rate and partial current density are in the order of $Li^+ > Na^+ > K^+$. (**B**) FE follows the same order of $Li^+ > Na^+ > K^+$. Data are shown for polarization potentials at −1.19, −0.99, and −0.79 V versus RHE.

O-etched CNS (fig. S14A) is simpler, lacking the low-energy emission from the sharp tips and appearing much more like a flat surface, although the WF (3.00 eV) is still significantly lower than that of the glassy carbon control (4.49 eV; fig. S14B) and published values for highly ordered pyrolytic graphite (*37*). The glassy carbon control was measured at the same time as the unemersed pristine and O-etched CNS. The apparent simplification of the UPS spectrum for O-etched CNS may therefore be due to blunting of the tips or oxidation of the surface carbon atoms during the O-etching process that would be expected to raise WF (*38*). C1s XPS measurements of the same O-etched sample indicates a significant contribution from carbonate-type functional groups, which is a reasonable result from O-etching of a carbon surface, and reflects partially oxidized graphene. Because pure graphite is unreactive with N_2, as evidenced by the glassy carbon control, we expect that this oxidation of the O-etched sample is less impactful than the loss of sharp tips with regard to the reduced ammonia production rate of the O-etched control.

The role of counterions

We investigated the role of electrolyte counterions by comparing Li^+, Na^+, and K^+ perchlorates. As shown in Fig. 3A, the formation rate (R_{NH3}) and partial current density (J_{NH3}) were the highest at all voltages for Li^+ and dropped with increasing cation size. FEs followed the same trend as formation rates (Fig. 3B). This trend may be plausibly ascribed to the steric effect of the counterions and the relatively strong interaction between counterions and N_2. The size of counterions increases in the order of $Li^+ < Na^+ < K^+$. Using eq. S2, it is straightforward to show that the electric field at the tip of the CNS surface increases with reducing counterion size as a result of the gradually reduced double-layer thickness, meaning that Li^+ is the best counterion in enhancing the electric field at the sharp spikes. In addition, the Li^+-N_2 interactions are reported for N_2 adsorption on Li^+ zeolites to have a binding energy in the order of 10 kcal mol^{-1}, which we ascribed to the interaction between Li^+ and the strong quadrupole moment of N_2 (*20*, *21*). The stronger adsorption of N_2 than O_2 over Li^+ in zeolites is exploited for the separation of N_2 from air (*39*, *40*). The binding energies of alkali metal ions with N_2 in the gas phase follow the order $\Delta E(Li^+) > \Delta E(Na^+) > \Delta E(K^+)$ (*20*, *21*). One of the limitations in nitrogen electrochemical conversion in aqueous electrolyte is the low solubility of N_2 in water. We hypothesize that the Li^+ cations electrostatically enriched in the Stern layer interact with the dissolved N_2 molecules in a similar manner to provide higher concentrations of N_2 at the electrode surface than in the electrolyte. This does not, however, preclude the alternative possibility that counterions interact with N_2's induced dipole moment. The positive correlation in Fig. 3 suggests that the smaller counterions may enhance the electric field in the Stern layer and increase the association between counterions and N_2 molecules, both of which promote the N_2 reactivity in a concerted way. It is essential to understand the solvation effects on both counterions and N_2 molecules in future studies.

To simulate the electric double layers at the tip of a CNS, we adopt a simulation system (details in the Supplementary Materials) as shown in fig. S3 (A and B). We used a carbon nanosphere with a radius of 1.0 nm to mimic the sharp tip of a CNS. The molecular dynamics simulations reveal a hybrid and complicated double-layer structure. Figure S3C shows the distribution of water molecules, Li^+ ions, and surrogate Cl^- ions as a function of the radial distance from the surface of the carbon nanosphere. The surface charges on the carbon nanosphere are screened partly by a layer of solvated Li^+ counterions located at ca. 0.36 nm from the carbon surface and also partly by a layer of desolvated Li^+ counterions located at ca. 0.20 nm from the carbon surface. Therefore, the effective thickness of the electric double layer is between 0.2 and 0.36 nm. The desolvated Li^+ counterion layer may serve to restrict the approach of water molecules to the electrode surface to reduce competitive hydrogen evolution reaction, thereby raising the FE of N_2 electroreduction.

^{15}N isotopic labeling

The CNS is doped with N atoms at approximately 5%; thus, to rule out the possibility that NH_3 was produced from the N dopant in the CNS catalyst rather than N_2 gas, we carried out two control experiments. First, a 6-hour electroreduction with argon gas rather than N_2 yielded no ammonia formation (also shown in Fig. 2A). Second, we conducted a 6-hour electrochemical reduction fed with 98% ^{15}N-enriched N_2 gas (alongside a control of $^{14}N_2$ gas), followed by the quantification of $^{15}NH_3$ and $^{14}NH_3$ with a phenylphenol ammonia quantification protocol (see Materials and Methods). Subsequent trimethylsilyl derivatization followed by gas chromatography–mass spectrometry (GC-MS) analysis (*41*) identified two major silylated products from natural ^{14}N and enriched ^{15}N, corresponding to double and triple silylation. The fragmentation patterns were identical, except that for ^{15}N product, the ^{15}N-containing fragments were shifted by +1 *m/z* (mass/charge ratio) compared to ^{14}N fragments. Figure S15 shows the mass spectra of double-silylated products, with the corresponding difference in the molecular ion at 497.3 and 498.3 *m/z*, respectively. Figure S16 shows an overlay of both ^{14}N and ^{15}N spectra in the region of the molecular ion (M^+). The ratios of the integrated areas of the molecular ion of the enriched versus natural abundance *m/z* increased from 0.56 to 48.73 for the triple-silylated product and from 0.47 to 9.43 for the more abundant double-silylated product. From these experiments, we conclude that the ammonia produced by this reaction is entirely from dissolved N_2 and not from N liberated from the CNS.

Energy efficiency and reaction rate limits

Ammonia is currently produced on a large scale using the Haber-Bosch process. The Haber-Bosch process has an energy efficiency of approximately 55%, calculated as (high heating value)/(total energy input including natural gas and electricity) (*42*, *43*), which we achieved using multiple passes through a reactor that has a single-pass yield of 15%. Although the energy efficiency of the process is high, capital costs are significant due to the pressures and temperatures required, and the process still emits greenhouse gases. In comparison, the electric energy consumed for the electrochemical reaction reported here can be calculated by

$$W = \int UI\,dt \tag{4}$$

where W is the total electric energy, U is the full cell potential (3.05 V), I is the overall current, and t is the reaction time. The actual energy efficiency of the electrochemical reaction is then estimated to be 5.25% at the current FE of 11.56% with a maximum theoretical energy efficiency of 45.9% if hydrogen evolution can be completely suppressed (FE, 100%). This comparison should be made in light of the fact that the Haber-Bosch process is generally exothermic and a significant amount of the energy in the process originates as chemical energy from methane, whereas an electrochemical process is entirely endothermic and driven by electricity, which can be renewable. Because of the inherent low reactivity of N_2, the reaction rates for the various reported means of electrochemical NH_3 production are still far too low for practical use.

Electrochemical processes for ammonia production, including this one, still need significant improvement in both yield and reaction rate before considering commercial application. However, the mechanism described here does offer high theoretical efficiency and will inform future studies.

CONCLUSION

In summary, we have demonstrated the electrochemical reduction of inert N_2 to ammonia by using N-doped CNS as the active electrode material. Because of the absence of transition metals on CNS, the reaction likely depends on a physical mechanism, associated with the enhanced electric fields arising from the sharp texture. This is supported by the O-etched CNS control experiment in which the blunt tips produce little ammonia under the same electrochemical conditions. The choice of counterions in the aqueous electrolyte is also critically important, with the ammonia production rates in the order of $Li^+ > Na^+ > K^+$, suggesting a favorable role for the smallest counterions in enhancing the electric field at the sharp spikes and increasing N_2 concentration within the Stern layer. In addition, the evolution of H_2 gas is suppressed by the formation of a dehydrated cation layer surrounding the tip, which helps to exclude water while allowing access of the N_2 molecule to the high electric field. Although further details require elucidation to fully understand this reaction mechanism, including the energetics of electron injection to N_2, solvation of both counterions and the N_2, elementary reaction steps for the six sequential electron and proton transfers, and the electric double layer structure with Li^+ and N_2 enrichment, this work establishes a viable physical catalytic reaction mechanism for electrolysis of N_2 to ammonia.

MATERIALS AND METHODS

Preparation of CNS

CNS was prepared by PECVD. The CNS can be grown on any conductive surface. Here, n-type 100-mm Si wafers ⟨100⟩ with As-doping (<0.005 ohm) were used as substrates. DC plasma was generated between the substrate (cathode) and the showerhead (anode) in a continuous stream of C_2H_2 and NH_3 gas, flowing at 80 and 100 standard cubic centimeters per minute, respectively, at 650°C for 30 min. The total pressure was maintained at 6 torr with a plasma power of 240 W.

Electrode preparation

To prepare the electrode from CNS grown on Si wafer, we gently scratched the surface of CNS at the edge of a piece of cleaved 1.0-cm × 1.5-cm CNS-coated wafer, and a small piece of indium metal (>99.99%; Alfa Aesar) was pressed on the scratch to produce an ohmic contact. Then, silver paste (Ted Pella) was used as conductive glue between a copper wire and the indium pad. The edges and backside of the samples were protected by epoxy to isolate them from contacting the electrolyte.

Materials characterization

SEM (Zeiss Merlin VP) and transmission electron microscopy (TEM) (Zeiss Libra 120 Plus; aberration-corrected STEM, Nion U100) were used for imaging and elemental analysis of the thin films. Representative TEM images are shown in fig. S1 for a film grown on a TEM grid for analytical purposes. Representative SEM images of CNS surface are shown in fig. S5. The side view images of CNS were illustrated in fig. S6. XPS measurements of the C1s region for both pristine and O-etched CNS were made at beamline 9.3.2 of the Advanced Light Source.

WF measurement

WF measurements on a range of samples were performed using UPS. Emersed electrodes of about 1 cm × 1 cm were prepared using reaction conditions identical to the electrochemistry described below. Electrodes were allowed to soak in N_2-saturated 0.25 M $LiClO_4$ before the application of the emersion potential. After a few minutes to equilibrate, the electrodes were emersed at potential into an argon blanket. The CNS was slightly hydrophilic, so any drops that were clinging to the surface were quickly blown off with argon while still at potential. The electrodes were then allowed to dry under flowing argon before removal to the UPS chamber. The electrodes were briefly exposed to air during the loading process; however, according to numerous literature reports, the double layer should be stable upon drying. WFs were measured using the secondary cutoff energies in UPS. He (I) radiation was generated by a SPECS UVS 300 source, and photoelectrons were detected by a SPECS 150 hemispherical analyzer operated in low angular dispersion mode. Samples were biased at −1.5, −3.0, and −4.5 V to allow low-energy electrons to be detected, to minimize energy distortions, and to establish reproducibility.

Electrochemistry

An H-shape electrochemical cell with a porous glass frit to separate the working and counter electrode compartments was used for N_2 electrocatalytic experiments. The cell maintained the working electrode parallel to the counter electrode to achieve a uniform voltage. N_2 (99.999%; Praxair), regulated by a mass flow controller (MKS Instruments) at 20 ml min^{-1}, flowed through the cell during the electrolysis. N_2 flow through the cell was needed to see large current efficiencies for N_2 reduction products, presumably because of mass transport limitations in a quiescent cell. The flow rate of 20 ml min^{-1} was chosen to ensure sufficient N_2 transport to the surface while preventing interference from gas bubbles striking the surface. The N_2 was humidified with water by passing it through a bubbler before it entered the electrolysis cell to minimize the evaporation of electrolyte. For each electrolysis experiment, the cell was assembled with CNS as the working electrode and platinum as the counter electrode. An Ag/AgCl electrode was used as the reference. A 0.25 M solution of $LiClO_4$ (99.99% metals basis; Sigma-Aldrich) was prepared with deionized water (18.2 megohm·cm) from a Millipore system and used as the electrolyte. Each compartment of the H cell contained 12.5 ml of electrolyte. As a control, identical experiments were conducted using other aqueous electrolytes containing $NaClO_4$ and $KClO_4$.

All electrochemical results are reported using the ECSA. Electrolysis was carried out with a Bio-Logic VSP potentiostat (VMP3), using CA and CP methods. Conversion of electrode potential versus RHE was calculated by $E_{RHE} = E_{Ag/AgCl} + 0.059 \times pH + E^{\circ}_{Ag/AgCl\ (Sat.)}$. EC-Lab software was used to link different techniques without returning to open circuit for each electrolysis experiment. To generate detectable amounts of products, we applied the electrolysis potential for 5 to 6 hours in a typical experiment and for 100 hours for the stability test.

Product quantification

The ammonia quantification protocol was adapted from EPA Standard Method 350.1. The protocol was applied to the electrolyte after electrolysis to determine and confirm the ammonia formed from N_2 reduction. Typically, 1.5 ml of electrolyte was pipetted into a glass vial. Then, 100 μl of 500 mM phenol and 50 μl of 2 mM sodium nitroprusside aqueous solution were added, followed by 100 μl of 700 mM sodium hypochlorite with 1 M NaOH aqueous solution. The mixture was gently agitated for 30 s and was then allowed to stand for 30 min

to ensure complete color development. The absorbance at 640 nm was measured with an ultraviolet-visible (UV-Vis) spectrometer (Varian Cary 5000).

To account for ammonia in the electrochemical cell headspace, we passed the cell exhaust gas through a 15 ml of 0.5 M H_2SO_4 solution to strip gaseous ammonia, if any. The pH of the solution in the acidic trap was firstly adjusted to neutral with 1 M NaOH, and then, the ammonia quantification protocol as described above was used to quantify the trapped ammonia from the overhead space of the electrochemical cell. Every sample was analyzed in this manner; however, no ammonia was detected, indicating that the product remained dissolved in the electrolyte.

A modified ammonia quantification protocol was identical to the above described method, except that *o*-phenylphenol was used instead of phenol. This resulted in a dye that was soluble in hexanol to extract the dye from the electrolyte for GC-MS analysis of isotopically labeled NH_3.

Absorbance measurements were calibrated by regression analysis of data obtained with standard ammonium-nitrogen solutions with concentration of 0, 2, 5, 10, 20, 50, 100, 250, and 500 μM NH_3-N liter^{-1} in $LiClO_4$ aqueous solutions. First, a concentrated standard ammonium-nitrogen solution containing 5 mM was prepared by dissolving 0.2675 g of ammonium chloride in 500 ml of 0.25 M $LiClO_4$ solution in a volumetric flask. Working standards were prepared by diluting the concentrated standard with 0.25 M $LiClO_4$ solution to obtain desired concentrations. Then, the ammonium chloride was converted to indophenol, as described above, and the absorbance was measured at 640 nm by UV-Vis spectrometer. Regression equations were used to convert absorbance values for electrolyte to NH_3-N concentrations. Two regression equations were obtained to determine low-concentration samples (0 to 50 μM) and high-concentration samples (0 to 500 μM), as shown in fig. S4. The slope is 0.00296 μM^{-1} for low concentration samples and 0.00291 μM^{-1} for samples with higher NH_3-N concentration.

The rate of ammonia formation was calculated using the following equation

$$R_{NH_3} = \frac{[NH_3] \times V}{t \times A} \quad (5)$$

where $[NH_3]$ is the measured NH_3 concentration, V is the volume of the electrolyte, t is the electrolysis time, and A is the ECSA of the working electrode.

To test the stability of the electrolysis on CNS, we monitored the formation of NH_3 over 100 hours. After a period of time, for example, 0.5, 1, 2, or 4 hours, 1.5 ml of the electrolyte was sampled by a syringe followed by introducing 1.5 ml of degassed $LiClO_4$ into the cell to maintain the electrolyte level in the electrochemical cell. The concentration of NH_3 was determined by the quantification protocol described above. The rate of ammonia formation at the time of sampling was calculated using the following equation

$$R_{NH_{3_n}} = \frac{[NH_3]_n \times V + \sum_{i=1}^{n-1} [NH_3]_i \times 1.5\ \text{ml}}{t_n \times A} \quad (6)$$

where n is the serial number of sampling, $[NH_3]_n$ is the measured NH_3 concentration, V is the volume of the electrolyte in the cell, t_n is the total time from the beginning to sampling, and A is the ECSA of the working electrode.

Mass spectrometry of ^{15}N product

The nitrogen source for ammonia was verified by GC-MS. *O*-phenylphenol was used in a modified version of the ammonia quantification reaction with isotopically enriched ^{15}N labeled ammonia, and natural ^{14}N ammonia, to form hexanol-soluble dye. The dye was silylated to facilitate separation and analyzed via GC-MS (Agilent 7890A/5975C inert XL GC-MS with Restek Rtx-5MS w/Integra-Guard column).

SUPPLEMENTARY MATERIALS

Supplementary material for this article is available at http://advances.sciencemag.org/cgi/content/full/4/4/e1700336/DC1

Modeling and simulation details

table S1. Elemental analysis of C, N, O, and Si in original CNS, O-etched CNS, and glassy carbon by energy dispersive x-ray spectrometry elemental mapping.

table S2. Partial current densities (mA cm^{-2}) for CNS, oxygen-etched CNS, glassy carbon, and CNS with argon gas.

table S3. Comparison of open-circuit potentials and polarizations of original CNS, O-etched CNS, and glassy carbon in 0.25 M $KClO_4$.

fig. S1. Representative TEM images of the CNS electrode.

fig. S2. The variation of surface electric field E_s calculated along the normal direction at the tip of a CNS for different tip radii in the case of desolvated Li^+ counterion and of solvated Li^+ counterion.

fig. S3. Molecular dynamics simulation of electric double layers near a carbon nanosphere immersed in LiCl solution.

fig. S4. Regression curves for ammonia quantification.

fig. S5. SEM micrographs of CNS surface.

fig. S6. SEM micrographs for the side view of CNS.

fig. S7. XPS spectra of CNS.

fig. S8. The overall current density (red curve) and formation rate (blue dots) with time at −1.19 V versus RHE.

fig. S9. CP experiment to investigate stability of the electrode during the initial 5 hours of the reaction, using a larger (4.8 cm^2) electrode to observe changes with respect to electrolyte composition.

fig. S10. Oxygen-etched CNS showing smoother texture compared to unetched CNS.

fig. S11. Correlated orbital levels calculated for three outer valence orbitals and three virtual orbitals at the level of EPT/aug-cc-pVTZ as a function of electric field strength.

fig. S12. Ultraviolet photoelectron spectroscopy and work functions of emersed CNS.

fig. S13. Ultraviolet photoelectron spectroscopy of pristine, unemersed CNS.

fig. S14. Ultraviolet photoelectron spectroscopy of O-etched CNS and glassy carbon.

fig. S15. Mass spectra of double-silylated product for ammonia from electrochemical N_2 reduction.

fig. S16. Mass spectra of ^{14}N and ^{15}N products in the mass region of the molecular ion.

References (*44*–*54*)

REFERENCES AND NOTES

1. U.S. Geological Survey, *Mineral Commodity Summaries 2016* (U.S. Geological Survey, 2016).
2. C. H. Christensen, T. Johannessen, R. Z. Sørensen, J. K. Nørskov, Towards an ammonia-mediated hydrogen economy? *Catal. Today* **111**, 140–144 (2006).
3. R. R. Schrock, Catalytic reduction of dinitrogen to ammonia by molybdenum: Theory versus experiment. *Angew. Chem. Int. Ed. Engl.* **47**, 5512–5522 (2008).
4. C. J. M. van der Ham, M. T. M. Koper, D. G. H. Hetterscheid, Challenges in reduction of dinitrogen by proton and electron transfer. *Chem. Soc. Rev.* **43**, 5183–5191 (2014).
5. D. Zhu, L. Zhang, R. E. Ruther, R. J. Hamers, Photo-illuminated diamond as a solid-state source of solvated electrons in water for nitrogen reduction. *Nat. Mater.* **12**, 836–841 (2013).
6. M. A. Shipman, M. D. Symes, Recent progress towards the electrosynthesis of ammonia from sustainable resources. *Catal. Today* **286**, 57–68 (2017).
7. S. Giddey, S. P. S. Badwal, A. Kulkarni, Review of electrochemical ammonia production technologies and materials. *Int. J. Hydrogen Energy* **38**, 14576–14594 (2013).
8. A. Tsuneto, A. Kudo, T. Sakata, Lithium-mediated electrochemical reduction of high pressure N_2 to NH_3. *J. Electroanal. Chem.* **367**, 183 (1994).
9. T. M. Pappenfus, K.-m. Lee, L. M. Thoma, C. R. Dukart, Wind to ammonia: Electrochemical processes in room temperature ionic liquids. *ECS Trans.* **16**, 89–93 (2009).
10. T. Murakami, T. Nishikiori, T. Nohira, Y. Ito, Electrolytic synthesis of ammonia in molten salts under atmospheric pressure. *J. Am. Chem. Soc.* **125**, 334–335 (2003).

11. S. Licht, B. C. Cui, B. H. Wang, F.-F. Li, J. Lau, S. Z. Liu, Ammonia synthesis by N_2 and steam electrolysis in molten hydroxide suspensions of nanoscale Fe_2O_3. *Science* **345**, 637–640 (2014).
12. F. Köleli, D. B. Kayan, Low overpotential reduction of dinitrogen to ammonia in aqueous media. *J. Electroanal. Chem.* **638**, 119–122 (2010).
13. R. Lan, J. T. S. Irvine, S. Tao, Synthesis of ammonia directly from air and water at ambient temperature and pressure. *Sci. Rep.* **3**, 1145 (2013).
14. L. Pospíšil, J. Bulíčková, M. Hromadová, M. Gal, S. Civiš, J. Cihelka, J. Tarábek, Electrochemical conversion of dinitrogen to ammonia mediated by a complex of fullerene C_{60} and γ-cyclodextrin. *Chem. Commun.* **2007**, 2270 (2007).
15. L. B. Sheridan, D. K. Hensley, N. V. Lavrik, S. C. Smith, V. Schwartz, C. D. Liang, Z. L. Wu, H. M. Meyer III, A. J. Rondinone, Growth and electrochemical characterization of carbon nanospike thin film electrodes. *J. Electrochem. Soc.* **161**, H558–H563 (2014).
16. Y. Song, R. Peng, D. K. Hensley, P. V. Bonnesen, L. B. Liang, Z. L. Wu, H. M. Meyer III, M. F. Chi, C. Ma, B. G. Sumpter, A. J. Rondinone, High-selectivity electrochemical conversion of CO_2 to ethanol using a copper nanoparticle/N-doped graphene electrode. *ChemistrySelect* **1**, 6055–6061 (2016).
17. J. Huang, B. G. Sumpter, V. Meunier, G. Yushin, C. Portet, Y. Gogotsi, Curvature effects in carbon nanomaterials: Exohedral versus endohedral supercapacitors. *J. Mater. Res.* **25**, 1525–1531 (2010).
18. A. I. Gerasimchuk, D. A. Zhogolev, Nonempirical calculation of the hydrogen, nitrogen, and oxygen molecules in the field of a strong point charge. *Theor. Exp. Chem.* **13**, 5 (1977).
19. M. Liu, Y. Pang, B. Zhang, P. De Luna, O. Voznyy, J. Xu, X. Zheng, C. T. Dinh, F. Fan, C. Cao, F. P. G. de Arquer, T. S. Safaei, A. Pepham, A. Kinkova, E. Kumacheva, T. Filleter, D. Sinton, S. O. Kelley, E. H. Sargent, Enhanced electrocatalytic CO_2 reduction via field-induced reagent concentration. *Nature* **537**, 382–382 (2016).
20. H. Mikosch, E. L. Uzunova, G. St. Nikolov, Interaction of molecular nitrogen and oxygen with extraframework cations in zeolites with double six-membered rings of oxygen-bridged silicon and aluminum atoms: A DFT study. *J. Phys. Chem. B* **109**, 11119–11125 (2005).
21. I. Papai, A. Goursot, F. Fajula, D. Plee, J. Weber, Modeling of N_2 and O_2 adsorption in zeolites. *J. Phys. Chem.* **99**, 12925–12932 (1995).
22. J. Duan, S. Chen, M. Jaroniec, S. Z. Qiao, Porous C_3N_4 nanolayers@N-graphene films as catalyst electrodes for highly efficient hydrogen evolution. *ACS Nano* **9**, 931–940 (2015).
23. I. Roger, M. D. Symes, Silver leakage from Ag/AgCl reference electrodes as a potential cause of interference in the electrocatalytic hydrogen evolution reaction. *ACS Appl. Mater. Interfaces* **9**, 472–478 (2017).
24. V. Kordali, G. Kyriacou, C. Lambrou, Electrochemical synthesis of ammonia at atmospheric pressure and low temperature in a solid polymer electrolyte cell. *Chem. Commun.* 1673–1674 (2000).
25. A. Sclafani, V. Augugliaro, M. Schiavello, Dinitrogen electrochemical reduction to ammonia over iron cathode in aqueous-medium. *J. Electrochem. Soc.* **130**, 734–736 (1983).
26. D. Wei, Y. Liu, Y. Wang, H. Zhang, L. Huang, G. Yu, Synthesis of N-doped graphene by chemical vapor deposition and its electrical properties. *Nano Lett.* **9**, 1752–1758 (2009).
27. E. Skúlason, T. Bligaard, S. Gudmundsdóttir, F. Studt, J. Rossmeisl, F. Abild-Pederse, T. Vegge, H. Jónsson, J. K. Nørskov, A theoretical evaluation of possible transition metal electro-catalysts for N_2 reduction. *Phys. Chem. Chem. Phys.* **14**, 1235–1245 (2012).
28. G. Ertl, Surface science and catalysis—Studies on the mechanism of ammonia-synthesis: The P.H. Emmett Award address. *Catal. Rev.* **21**, 201–223 (1980).
29. P. Stoltze, J. K. Norskov, Bridging the "pressure gap" between ultrahigh-vacuum surface physics and high-pressure catalysis. *Phys. Rev. Lett.* **55**, 2502–2505 (1985).
30. P. Wang, F. Chang, W. Gao, J. Guo, G. Wu, T. He, P. Chen, Breaking scaling relations to achieve low-temperature ammonia synthesis through LiH-mediated nitrogen transfer and hydrogenation. *Nat. Chem.* **9**, 64–70 (2017).
31. M.-T. Nguyen, N. Seriani, R. Gebauer, Nitrogen electrochemically reduced to ammonia with hematite: Density-functional insights. *Phys. Chem. Chem. Phys.* **17**, 14317–14322 (2015).
32. B. Delley, Vibrations and dissociation of molecules in strong electric fields: N_2, NaCl, H_2O and SF_6. *J. Mol. Struct.* **434**, 229–237 (1998).
33. T. Koopmans, Über die Zuordnung von Wellenfunktionen und Eigenwerten zu den Einzelnen Elektronen Eines Atoms. *Physica* **1**, 104–113 (1934s).
34. W. Hansen, D. Kolb, D. Rath, R. Wille, An ESCA study on emersed electrodes. *J. Electroanal. Chem. Interfacial Electrochem.* **110**, 369–373 (1980).
35. W. N. Hansen, D. M. Kolb, The work function of emersed electrodes. *J. Electroanal. Chem. Interfacial Electrochem.* **100**, 493–500 (1979).
36. A. T. D'Agostino, W. N. Hansen, Observation of systematic electrochemically induced binding energy shift in the XPS spectra of emersed Cs^+ double layer species. *Surf. Sci.* **165**, 268–276 (1986).
37. S. Axnanda, M. Scheele, E. Crumlin, B. H. Mao, R. Chang, S. Rani, M. Faiz, S. D. Wang, A. P. Alivisatos, Z. Liu, Direct work function measurement by gas phase photoelectron spectroscopy and its application on PbS nanoparticles. *Nano Lett.* **13**, 6176–6182 (2013).
38. P. V. Kumar, M. Bernardi, J. C. Grossman, The impact of functionalization on the stability, work function, and photoluminescence of reduced graphene oxide. *ACS Nano* **7**, 1638–1645 (2013).
39. R. V. Jasra, N. V. Choudary, S. G. T. Bhat, Separation of gases by pressure swin. *Sep. Sci. Technol.* **26**, 885–930 (1991).
40. V. N. Choudary, R. V. Jasra, T. S. G. Bhat, Adsorption of nitrogen-oxygen mixture in NaCaA zeolites by elution chromatography. *Ind. Eng. Chem. Res.* **32**, 548–552 (1993).
41. J. Kanda, Determination of ammonium in seawater based on the indophenol reaction with *o*-phenylphenol (OPP). *Water Res.* **29**, 2746–2750 (1995).
42. C. Zamfirescu, I. Dincer, Using ammonia as a sustainable fuel. *J. Power Sources* **185**, 459–465 (2008).
43. E. Worrell, D. Phylipsen, D. Einstein, N. Martin, *Energy Use and Energy Intensity of the US Chemical Industry* (Lawrence Berkeley National Laboratory, 2000).
44. A. L. Shimkevich, On arising nanohydrides in reduced alkaline solution. *Am. J. Modern Phys.* **2**, 185–189 (2013).
45. L. L. Zhang, X. Zhao, H. Ji, M. D. Stoler, L. Lai, S. Murali, S. Mcdonnel, B. Cleveger, R. M. Wallace, R. S. Ruoff, Nitrogen doping of graphene and its effect on quantum capacitance, and a new insight on the enhanced capacitance of N-doped carbon. *Energy Environ. Sci.* **5**, 9618–9625 (2012).
46. S. H. Lee, J. C. Rasaiah, Molecular dynamics simulation of ion mobility. 2. Alkali metal and halide ions using the SPC/E model for water at 25°C. *J. Phys. Chem.* **100**, 1420–1425 (1996).
47. W. L. Jorgensen, Optimized intermolecular potential functions for liquid alcohols. *J. Phys. Chem.* **90**, 1276–1284 (1986).
48. B. Hess, H. Bekker, H. J. C. Berendsen, J. G. E. M. Fraaije, LINCS: A linear constraint solver for molecular simulations. *J. Comput. Chem.* **18**, 1463–1472 (1997).
49. B. Hess, C. Kutzner, D. van der Spoel, E. Lindahl, GROMACS 4: Algorithms for highly efficient, load-balanced, and scalable molecular simulation. *J. Chem. Theory Comput.* **4**, 435–447 (2008).
50. J. Linderberg, Y. Öhrn, in *Propagators in Quantum Chemistry* (Wiley & Sons, ed. 2, 2004).
51. J. V. Ortiz, V. G. Zakrzewski, O. Dolgounitcheva, One-electron pictures of electronic structure: Propagator calculations on photoelectron spectra of aromatic molecules, in *Conceptual Perspectives in Quantum Chemistry*, J.-L. Calais, E. Kryachko, Eds. (Springer, 1997), pp. 465–517.
52. M. J. Frisch, G. W. Trucks, H. B. Schlegel, G. E. Scuseria, M. A. Robb, J. R. Cheeseman, G. Scalmani, V. Barone, B. Mennucci, G. A. Petersson, H. Nakatsuji, M. Caricato, X. Li, H. P. Hratchian, A. F. Izmaylov, J. Bloino, G. Zheng, J. L. Sonnenberg, M. Hada, M. Ehara, K. Toyota, R. Fukuda, J. Hasegawa, M. Ishida, T. Nakajima, Y. Honda, O. Kitao, H. Nakai, T. Vreven, J. A. Montgomery, Jr., J. E. Peralta, F. Ogliaro, M. Bearpark, J. J. Heyd, E. Brothers, K. N. Kudin, V. N. Staroverov, R. Kobayashi, J. Normand, K. Raghavachari, A. Rendell, J. C. Burant, S. S. Iyengar, J. Tomasi, M. Cossi, N. Rega, J. M. Millam, M. Klene, J. E. Knox, J. B. Cross, V. Bakken, C. Adamo, J. Jaramillo, R. Gomperts, R. E. Stratmann, O. Yazyev, A. J. Austin, R. Cammi, C. Pomelli, J. W. Ochterski, R. L. Martin, K. Morokuma, V. G. Zakrzewski, G. A. Voth, P. Salvador, J. J. Dannenberg, S. Dapprich, A. D. Daniels, Ö. Farkas, J. Foresman, J. Ortiz, J. Cioslowski, D. Fox, *Gaussian 09, Revision D. 01* (Gaussian Inc., 2009).
53. T. Trickl, E. F. Cromwell, Y. T. Lee, A. H. Kung, State-selective ionization of nitrogen in the $X^2\Sigma^+_g v_+=0$ and $v_+=1$ states by two-color (1+1) photon excitation near threshold. *J. Chem. Phys.* **91**, 6006–6012 (1989).
54. G. Wulfsberg, in *Inorganic Chemistry* (University Science Books, 2000), 521 pp.

Acknowledgments

Funding: The synthesis, materials science, and electrochemistry supporting this work were conducted at the Center for Nanophase Materials Sciences, which is a U.S. Department of Energy (DOE) Office of Science User Facility. This work used computational resources of the National Energy Research Scientific Computing Center, which are supported by the Office of Science of the DOE under contract no. DE-AC02-05CH11231. A portion of this research used resources of the Advanced Light Source, which is a DOE Office of Science User Facility under contract no. DE-AC02-05CH11231. **Author contributions:** A.J.R. conceived and led the experiment. Y.S. and D.J. performed electrochemistry. R.P, P.V.B., T.J.T., N.L.E., Z.W., D.A.C., M.C.H., A.P.B., and H.M.M. assisted with product characterization and catalyst analysis. D.K.H. synthesized the CNSs. L.L., J.H., F.Y., F.Z., R.Q., and B.G.S. carried out theoretical calculations and simulations. All authors contributed to the manuscript. **Competing interests:** A.J.R., D.K.H., and Y.S. are inventors on a provisional patent related to this work filed by UT-Battelle LLC (no. 62/508,023, Filed 18 May 2017). The authors declare that they have no other competing interests. **Data and materials availability:** All data needed to evaluate the conclusions in the paper are presented in the paper and/or the Supplementary Materials. Additional data are available from authors upon request.

Submitted 1 February 2017
Accepted 12 March 2018
Published 27 April 2018
10.1126/sciadv.1700336

Citation: Y. Song, D. Johnson, R. Peng, D. K. Hensley, P. V. Bonnesen, L. Liang, J. Huang, F. Yang, F. Zhang, R. Qiao, A. P. Baddorf, T. J. Tschaplinski, N. L. Engle, M. C. Hatzell, Z. Wu, D. A. Cullen, H. M. Meyer, B. G. Sumpter, A. J. Rondinone, A physical catalyst for the electrolysis of nitrogen to ammonia. *Sci. Adv.* **4**, e1700336 (2018).